The use of wavelet analysis to derive infiltration rates from time-lapse 1D resistivity records.

Adam Pidlisecky[1*] and Rosemary Knight[2]

[*]**Corresponding Author**

[1]University of Calgary, Department of Geoscience
2500 University Dr NW
Calgary, AB, Canada
T2N-1N4
Email: adampid@ucalgary.ca
Phone: 403-220-6679

[2]Stanford University Dept. of Geophysics
397 Panama Mall
Stanford, CA, USA
94305-2215
Email: rknight@stanford.edu
Phone: 650-736-1487

submitted to Vadose Zone

March 13,2010

Revisions submitted

July 7, 2010

Abstract

As part of a study to understand factors impacting the efficiency of an artificial recharge pond in Watsonville, CA, a time-series of resistivity measurements were made using a permanently installed 1D resistivity probe. Measurements were made in the top 2m of sediment with data acquired every 30 minutes. There was an observed diurnal signal in these data, due to daily temperature fluctuations in the pond water. By viewing this signal as a thermal tracer we use the movement of the associated thermal front to estimate infiltration rates from the resistivity data. We present a wavelet-based method for calculating lagtimes of the thermal front, between measurement locations. As part of this algorithm, we test the statistical significance of a given signal, and automatically reject calculated lagtimes that are associated with signals below a given confidence interval. We include a linear inversion routine for calculating the velocity of the thermal front from the calculated lagtimes. Using the thermal velocity, we estimate an infiltration rate at the resistivity probe that decreases from approximately 3.5 m/day, to 1 m/day, over a period of 18 days. Resistivity data have a distinct advantage over direct temperature measurements: a resistivity measurement is sensitive to changes outside the region disturbed by instrument emplacement. While our processing approach is demonstrated on the presented resistivity data, it is equally valid for use with direct temperature measurements.

1. Introduction

A growing component of water resource management is the development of systems for the subsurface storage and subsequent recovery of water. At many locations throughout the western U.S., this is accomplished through the use of recharge ponds. A recharge pond is filled with water during the months when there is available surface water; the pond water percolates into the subsurface; the water is then recovered at other times of the year to supplement the supply of surface or groundwater. Central to the successful operation of such a system is the need for information about the subsurface processes and properties that govern the quantity and quality of stored and recovered water. In the southwestern U.S. there are several recharge ponds that have been the focus of long-term studies (e.g. Izbicki et al, 2007; Izbicki et al 2008).

One critical process in the use of a recharge pond is the infiltration of the pond water into the subsurface. In the operation of most ponds, there is a limited period of time (e.g. the rainy season) when the pond can be filled with water and the subsurface storage region recharged. During that time period the challenge is to ensure that sufficient pond water infiltrates so as to maximize subsurface storage; this requires maintaining an optimal infiltration rate. In this study, we are working at the Harkins Slough recharge pond, located approximately 5 km west of Watsonville, California and 1 km from the coast. The infiltration rate in the pond has been found to decay rapidly with time, thus significantly limiting the amount of stored water. The cause of this decay is presumed to be clogging of the pore space through which the water percolates, due to the accumulation of fines and/or the build-up of biomass associated with microbial activity.

The method currently used to determine the infiltration rate at the base of the pond is a simple mass balance, where the pumping rates for adding water to the pond, and the measured changes in the height and areal extent of the pond are used to provide a pond-scale average (Racz et al., 2008). As such this measure of infiltration contains no detailed information about the spatial and temporal variability in infiltration rate across the base of, or underlying, the pond. However, this is the level of detail that is needed in order to determine the operational changes that could be made to reduce or eliminate the decay in infiltration rate, and thus increase the volume of stored water. The objective of our research is to use measurements of electrical resistivity, in the ~2 m below the pond, as a means of better understanding the subsurface controls on infiltration rates.

Electrical resistivity measurements are well-suited for this application. The near-surface geological material underlying the pond is predominantly well-sorted, medium- to coarse-grained sand. The link between measurements of electrical resistivity and the properties of near-surface materials has been the subject of numerous laboratory and theoretical studies, as reviewed in detail in Lesmes and Friedman (2005) and Knight and Endres (2005). In a clean sand, the dominant mechanism of electrical conduction is ionic conduction through the pore fluid. The changes in electrical resistivity, in the region below the pond, will therefore be determined by changes in the volume of the water present in the sands, the salinity of the water, and/or the temperature of the water. In this study we acquire resistivity data using a probe emplaced in the bottom of the pond. We focus on isolating the component of the resistivity data that captures the change in temperature of the infiltrating pond water, and from that estimating infiltration rates. When making measurements using an emplaced subsurface measurement device (such as a probe), there is a key advantage to using resistivity measurements, rather than thermistors or thermocouples, to determine temperature. The direct-temperature sensors are point measurements, and as such can be significantly affected by the disturbed zone immediately adjacent to the device. Electrical resistivity measurements are not point measurements, but volume averages, that are sensitive to the properties away from the measurement device.

Temperature fluctuations, obtained from point measurements, have been used to infer infiltration rates through either numerical modeling, (e.g., Constantz and Stonestrom, 2003;

Constantz, 2008) or time-series analysis (e.g., Hatch et al., 2006, Keery et al., 2007). In this work we build on the time-series approach of Hatch et al. (2006), which had previously demonstrated the use of signal analysis of temperature records for determining infiltration rates. In their work, diurnal temperature fluctuations acted as a periodic temperature forcing and streambed infiltration rates were estimated from time-series analysis of vertical temperature profiles. Our field experiment allowed us to assess the use of vertical profiles of electrical resistivity measurements as an alternative or complementary means of monitoring and quantifying infiltration rates.

In this paper, we: 1) present evidence for a measureable diurnal temperature signal in resistivity records, 2) present a wavelet-based method for calculating lagtimes of the associated thermal front between measurement locations, and 3) develop a linear inversion routine for calculating the velocities of the thermal front, based on the calculated lagtimes. Finally, we apply the approach of Hatch et al. (2006) to convert these thermal velocities to infiltration rates. While our processing approach is demonstrated on the presented resistivity data, it is equally valid for use with direct temperature measurements, and can be applied to either data set without modification of the approach.

2. Site

The Harkins Slough recharge pond, which has been in operation since the fall of 2001, was designed and constructed by CH2M Hill and is owned and operated by the Pajaro Valley Water Management Agency (PVWMA). The oval-shaped pond, depicted in Figure 1, is approximately 300 m by 100 m. It has a shallow outer bench, approximately 1.5 m deep, and when full reaches a depth water depth of 5 m at the deepest point. During winter storms, overland flows drain into Harkins Slough, which is surrounded by agricultural fields. A small portion of the flow through the slough (a maximum of 2,000 acre-feet or approximately 2.5 x 10^6 m^3 each winter between November 1 to May 31) is diverted and pumped into the recharge pond. The pond is filled with water during the winter months (typically January to May); the water percolates through the base of the pond and is stored in the underlying aquifers. Water is retrieved from recovery wells around the pond throughout the year to supplement the delivered water supply and reduce the groundwater needs of the local farmers in this coastal zone. The pond, when full, can hold approximately 44 acre-feet (5.4 x 10^4 m^3) of water, and has had recorded volumetric infiltration rates exceeding 20 acre-feet/day (2.47 x 10^4 m^3.) However, due to the decrease in infiltration rate PVWMA was only able to infiltrate approximately 800 acre-feet (approximately 1 x 10^6 m^3) during the 2008 operation year (from January to May.)

Figure 1 A map view schematic of the Harkins Slough recharge pond, showing approximate locations of the water inlet and resistivity probe. The dashed contour represents the approximate boundary between the shallow outer bench and the deeper inner section. The outer solid boundary denotes the edge of the pond.

3. Electrical resistivity measurements

In order to monitor the infiltration processes at the pond, we developed an inexpensive 1D resistivity probe designed for measuring changes in subsurface electrical resistivity. The probe, made of 3 m PVC pipe, was equipped with 35 stainless steel electrodes, evenly spaced at 8.5 cm intervals. The probe was installed near the center of the pond in December 2007, with the top meter left above the ground to provide a measure of the electrical resistivity of the pond water. The probe was connected to an autonomous monitoring system, with data being acquired every 30 minutes for the duration of pond operation, from January to March 2008.

Electrical resistivity measurements involve injecting current I through one pair of electrodes and measuring the drop in potential ΔV between another pair of electrodes. Measurements were made using a standard 4-electrode Wenner array; for 35 electrodes, this yields 32 unique measurements of resistance R, where $R = \frac{\Delta V}{I}$. When the current is injected, the surrounding 3-D resistivity structure determines the potential that will be measured at all locations for a given input current. In order to obtain true resistivity values, we are required to invert these measurements, however, we can easily calculate the apparent resistivity which provides an estimate of the in-situ resistivity. The apparent resistivity ρ_{app} is calculated using equation 1:

$$\rho_{app} = K \cdot \frac{\Delta V}{I} \tag{1}$$

where K is the geometric factor, which is specific to each measurement location. The calculation of K is trivial, requiring only electrode locations and the location of the free surface (see, for example, Telford et al., 1990). With an apparent resistivity calculated at each depth, we produced a depth-time plot of electrical resistivity below the pond as shown in Figure 2.

Figure 2 Time series of 1-D apparent resistivity data. 0 on the depth axis indicates the pond bottom (indicated by the dashed line), while negative values indicate height above pond bottom.

Figure 2 shows the apparent resistivity record from the probe. Depth equal to 0 corresponds to the bottom of the pond, with positive depth values indicating increasing depth. The main feature in the figure is the significant change in the measured apparent resistivity seen at 300 h in the pond water (shown at depths less than 0 m) and seen several hours later moving into the subsurface (shown at depths greater than 0 m). Within the first 300 hours of pond operation, the apparent resistivity of the pond water was at its lowest values, i.e. the pond water was the most conductive. This is to be expected, as this was water from the first major storm of the year, which washed residual fertilizers and salts, as well as fine-grained sediments, from local agriculture fields and hence, had a higher fraction of dissolved and suspended solids than water arriving later in the winter. In fact, pumping was stopped between approximately 200-300 h, as the water was too turbid to be suitable for infiltration. Corresponding to the time that pumping was resumed at approximately 300 h, we see a large increase in fluid apparent resistivity; as the rains continued, the ground surface within the watershed became progressively cleaner. This change in apparent resistivity can be tracked into the subsurface data in Figure 2.

Figure 3 (a) A single apparent resistivity time series from a depth of -0.5m (i.e. middle of the water column); (b) Temperature time series from a depth of ~ -0.5m.

We can inspect the changes in apparent resistivity in the pond water in more detail by displaying, as is done in Figure 3a, a plot of the apparent resistivity signal at one measurement location in the water column (from a depth of -0.5 m in Figure 1). In addition, we present a temperature time series in Figure 3b, of the temperature of the pond water obtained using the Hobo tidbit temperature sensor also located 0.5 m above the pond bottom. The large-scale variations in the apparent resistivity of the pond water, seen in Figure 2, is also seen here in Figure 3a. There was initially a decrease in apparent resistivity in the first few hours as the water, containing relatively high amounts of dissolved and suspended solids, entered the pond; resistivity then stayed relatively constant until the jump in the fluid apparent resistivity, clearly seen just after 300 h, when the pump was re-started. There was a decrease in the temperature of the pond at this point, suggesting that the change in apparent resistivity was due to a combination of temperature and salinity effects and likely reflects the influx of fresher, colder water. Between 400 and 600 hours there was a gradual increase in apparent resistivity. Because temperature was relatively constant over this time period we conclude that the dominant factor controlling the general trend in apparent resistivity during this time period was the decreasing salinity of the pond water; i.e. the pond water was becoming progressively cleaner. Around 650 hours the trend reversed and there was a gradual decrease in apparent resistivity. As can be seen in Figure 3b, this corresponds to a trend in increasing water temperature in the pond. This increase in temperature was due to atmospheric forcing as a warm front moved into the region. Using an estimate of a 2% change in fluid resistivity per degree Celsius, (Brassington, 1998) we would expect to see a decrease in electrical resistivity of approximately 6% for the time window between 650 h and 800 h (assuming fluid salinity is constant). This estimate corresponds well with the observed decrease, in Figure 3a, of approximately 7%. We suggest that in this time window, where pumping rates are constant and there is no precipitation, long time scale (greater than 2 h) temperature changes are the dominant drivers of apparent resistivity changes.

What is of interest in Figure 3b are the diurnal temperature fluctuations that are seen throughout the entire record. When we consider the resistivity data shown in Figure 3a, we see this diurnal signal between 650 hours and 950 hours, captured as fluctuations in the magnitude of the apparent resistivity. We note that while the diurnal signal is particularly clear during this interval, it is present at some earlier times in the image. At this earlier time, the fluctuations at lower resistivity values are masked in the plot by the large overall range of resistivity values.

Our review of the resistivity data led us to conclude that there were two variables, the salinity and temperature of the pond water, which caused the observed changes in the electrical resistivity at both large and small temporal scales. The change in the salinity and the change in mean daily temperature of the pond water both resulted in changes in resistivity on temporal scales on the order of 10's to 100's of hours. The diurnal temperature fluctuation resulted in changes in resistivity at a smaller temporal scale, on the order of ~24 h.

4. Processing: Isolating the diurnal resistivity signal

Motivated by prior work focused on using temperature signals to infer infiltration rates through time-series analysis (e.g. Hatch et al., 2006; Keery et al., 2007), we developed an approach for capturing, and using, the diurnal signal in the resistivity data to quantify infiltration rates. By measuring the lagtimes of the associated thermal front as a function of depth, we can estimate the infiltration rate at the probe location. Figure 4 schematically depicts this. As the alternating warm and cold phases propagate in the subsurface we can measure this signal using absolute temperature, or electrical resistivity. As seen in the image, a given thermal front (due to diurnal heating or cooling) will arrive at a near-surface sensor earlier in time than at a deeper measurement location. By calculating the lagtime between these two locations, we can obtain the velocity of the thermal front.

Both resistivity and temperature records are non-stationary. Recent work by Henderson et al., (2009) demonstrated the use of wavelets for analysis of temperature data from distributed temperature sensors. In addition to the work of Henderson et al. (2009), wavelets have seen use in the hydrologic sciences by Labat (2008, 2010) for analyzing large-scale fresh water stream discharge. These works highlight the fact that wavelet processing is useful when signals are non-stationary, and the frequency content of a signal needs to be localized as a function of time. We therefore adopted wavelet processing as the method for determining velocities of the thermal front.

Figure 4 A schematic of the thermal front propagating into the base of the pond. Red bars indicate warmer water, while blue indicate cooler water. At a given measurement location we will see a decrease or increase in the resistivity, corresponding to the warmer and cooler water, respectively. The measured signals at two different depths, as depicted by the dashed and solid lines, can be used to calculate the time it takes the thermal front to propagate between the measurement locations.

3.1 – Wavelets

The initial part of our workflow involves using wavelet analysis to identify regions of measurable/reliable diurnal signals. We then construct an image of the thermal front lagtime, as a function of depth and time. That is we produce images that display the time it took, relative to some reference point, for the thermal front to move from a defined reference depth.

Wavelet analysis is well-suited for dealing with non-stationary signals, such as those often encountered in geophysical data (such as the resistivity data from the pond). Wavelets are signals that are localized in both time and frequency; as such, they provide an excellent tool for characterizing the frequency content of a signal as a function of time. The use of, and theory behind, wavelets is well described in Kumar and Foufoula-Georgiou (1997) and Torrence and Compo (1998).

In this study we used the continuous wavelet transform (CWT), and the cross-wavelet transform (XWT). The CWT convolves a wavelet with a time-domain signal, as described by equation 2:

$$W_n^X(s)=\sqrt{\frac{\delta t}{s}}\sum_{n'=1}^{N} x_n \psi_0\left(\left(n'-n\right)\frac{\delta t}{s}\right) \tag{2}$$

where $W_n^X(s)$ is the transformed time series for a given scale s (e.g.. in our case the period (h) of the signal); x_n is the timeseries, δt is the time step; n is the time; and n' is reversed time (Grinsted et al., 2004). The function, ψ_0, is the wavelet function under consideration. There are several candidate wavelet functions, (Torrence and Compo, 1998). For this work we chose to use the Morlet wavelet; it is a complex function, so we can obtain both amplitude and phase information from its use. A power spectrum is produced from equation 2 by taking $|W_n^X(s)|^2$ and normalizing by the signal variance. This can be thought of as equivalent to a Fourier power spectrum; however with wavelets, there is no assumption of a periodic signal.

Figure 5a presents a CWT of the resistivity signal in the sediment underlying the pond at a depth of ~ 0.17 m. We note that with each depth there is an associated time series, and therefore a CWT. Shown on the figure is a dashed line corresponding to a period of 24 hours, the signal component of specific interest in this study. When calculating the CWT there is no padding of the temporal signal, as such there are edge effects at the beginning and end of each signal. The shaded regions on the left and right of the image indicate zones with edge effects in the CWT; the CWT is unreliable in this region. Also shown on this figure are the 95% confidence intervals (bold black lines). These confidence intervals are the results of a statistical significance test of the wavelet spectra conducted using the method described in Torrence and Compo (1998). The confidence intervals indicate that the signal contained within the contours has a 95% likelihood of being significant when compared to a CWT of a red-noise spectrum. Red-noise tends to have characteristics similar to many geophysical signals, as it has low frequency noise that has a larger amplitude than high frequency noise **(**Torrence and Compo, 1998)**.**

There are several key features to note in the CWT in Figure 5a. First, at approximately 300 h, there is a high-amplitude, wide-spectrum signal that swamps any diurnal fluctuations. This signal is coincident with the rapid jump in apparent resistivity at approximately 300 h. Between approximately 500 h and 950 h, there is substantial energy that is isolated around the 24-h period. This energy is of lower magnitude than the signal at ~300 h, but it is still judged to be statistically significant falling, as it does, within the 95% confidence internals.

Figure 5b is the CWT from within the sediments at a depth of 0.68 m. It is clear from this figure that the isolated diurnal signal decayed in late time (i.e. greater than 850 h) and was only above the 95% confidence interval between 500 h and 850 h. This was to be expected; the heat was dissipating with depth, so the measurable effect on resistivity was reduced. By inspecting Figure 5, we were able to use the CWT's to determine which regions in our time series contained significant 24-h signal.

Figure 5(a) CWT for the resistivity signal at a depth of 0.17 m; (b) CWT for the signal at a depth of 0.68 m. The dashed line indicates the 24 h period. The dark black contour indicates the 95% CI. The shaded region indicates areas with edge effects.

In order to generate an image of lagtime, as a function of depth and time, we needed to relate the signal from a given reference depth, to the signals at all other depths of interest. This was done using the crosswavelet transform XWT to determine the regions of the two CWT's with high coincident power. The XWT is calculated as follows:

$$W^{XY} = W^{X} W^{Y*} \quad (3)$$

where W^{XY} is the cross wavelet transform; W^{X} is the real component of the CWT for a reference time series (i.e. the time series at a given depth), and W^{Y*} is the complex conjugate of the CWT for another time series (i.e. in our case, the time series at some other depth). The power spectrum is defined as $|W^{XY}|^2$. A phase spectrum can by obtained by taking the phase angle between the real and complex portions of the XWT. We used the phase spectrum to calculate the lagtimes, for a given depth interval, as a function of time.

Figure 6 is the XWT for the signals from Figure 5, at depths of 0.17 m and 0.68 m. There is substantial energy, centered about the 24-h period, from 500 h to 900 h in the XWT for these two time series. In the image in Figure 6, the phase angle is denoted by arrows, with a zero degree lag indicated by an arrow pointing directly to the right, a 180-degree lag indicated by an arrow pointing to the left. As in Figure 5, the dark black line represents the 95% confidence interval. Note that the confidence interval extends to ~900 h; yet the CI for the individual time series from a depth of 0.68 m, as seen in Figure 5b, only extends to ~ 850 h. This highlights a problem with the determination of confidence intervals. It is possible to have energy in the XWT spectrum that satisfies the significance criterion outlined by Torrence and Compo, even if one of the individual CWT's does not satisfy this criterion at the given time/period. This issue was noted by Maraun and Kurths (2004) who suggested that it could be circumvented by using the measure of wavelet coherence, which is a XWT normalized by the product of the individual CWT's. While this is a viable alternate approach, there can be issues with the wavelet coherence measure when the CWT's have low amplitude (Maraun and Kurths, 2004). Given this, we have opted to use the XWT approach, with the caveat that the energy level in each of the individual CWT's be above the 95% confidence interval. We expect that a coherence measure would produce similar results.

Figure 6 XWT between depths of 0.17 m and 0.68 m. Arrows indicate the phase direction and magnitude. Arrows pointing to the right indicate 0 phase shift; arrows pointing to the left indicate a phase shift of π. The dashed line indicates the 24 h period. The dark black contour indicates the 95% CI.

Having calculated the XWT for a depth interval we were able to determine lagtime between the signals using the following (Grinsted et al., 2004):

$$\Delta t = \frac{\Delta \phi}{2 \cdot \pi \cdot T} \tag{4}$$

where Δt is the lagtime, $\Delta\phi$ is the phase lag, and T is the period under consideration. We searched for the maximium amplitude in the XWT, between a period of 23 and 25 hours, and determined the lagtime with this value. We used the signal from just below the pond bottom (depth = 0.17 m) as the reference trace for all the calculations. By choosing the reference trace as the uppermost trace we were able to obtain the best representation of the temperature signal at the water/sediment interface, before the signal had degraded with movement into the subsurface. In addition, calculating lagtimes from the pond bottom resulted in an integrated estimate of lagtime, which is less susceptible to noise.

The following are the three criteria that we used for accepting or rejecting a calculated lagtime:

1. **Broad band signal:** If the dominant signal (at a given time) was not isolated around the 24-h period we did not calculate a lagtime. While there might have been signal in the 24-h period, if it was not isolated we could not guarantee that it was due to the diurnal temperature fluctuations.

2. **Negative lag:** Our reference depth was selected to be at 0.17 m below the pond bottom. Invoking the argument of causality, if we calculated a negative timelag, indicating that the reference signal trailed the other signal, we rejected the data. We expected our thermal front to have propagated downward; therefore a negative timelag was impossible and taken to indicate low signal quality at a give depth/time.
3. **XWT confidence interval:** The XWT can have significant energy in a region where only one of the corresponding CWT's has significant energy. In order to overcome this issue, we rejected phase lags that were calculated at periods/time that 1) did not satisfy the significance criteria as determined from the XWT spectrum, or 2) did not satisfy the significance criterion for either of the individual CWT spectra.

Adhering to the above rules, we processed our filtered resistivity data to produce an image of lagtime, seen in Figure 7. This figure now spans the time window from 500 h to 900 h, the region that was deemed to have significant 24-hour signal; regions of white had no discernable signal. Upon qualitative inspection of the figure, two points are clear: 1) the lagtimes get larger to the right indicating that the infiltration rate is decreasing with time, and 2) at later times, where the lagtimes are longer, the signal quality decays (due to heat loss), and hence the vertical extent of measurable signal is much less.

Figure 7 Lagtime image. White areas indicate that the signal did not pass our acceptance criteria.

Of the approximately 1000-hour (~ 6-week) record presented in Figure 2, we were able to calculate lagtimes for approximately 40% of the recording period. The major factor that seems to influence our ability to use the diurnal signal in early time is that the pumping rates, and related pond height, are varying during the first 500 hours of operation. We surmise that this causes mixing in the pond that reduces the thermal signal. In particular, the rapid change in pond height occurs at approximately 300 hours, which is coincident with the broadband signal that is seen in Figure 6.

3.2 Inverting for thermal velocity from lagtime.

Processing the resistivity data, using the wavelet analysis described above, yielded a record of lagtime, as shown in Figure 7, as a function of measurement depth and time. We used these lagtimes to estimate the vertical velocity of the thermal front, referred to as the thermal velocity. Our approach involved formulating a linear inverse problem that allowed us to solve for thermal velocity as a function of time. We parameterized the forward model with a single thermal velocity at each time, for all depths. Obviously, one could choose a multi-layer model, where the thermal velocity varied with depth. However, we found that with a single layer model, we achieved a good data fit. Given that this simple model fit the data well, we felt there was no reason to introduce more model complexity. A more complex model can always fit the data, given the increase in degrees of freedom.

In order to invert the lagtime data, we first formulated a forward model at each time step. This model allows us, for a given thermal velocity, to estimate the lagtime at a given measurement depth. Equation 5 describes this model:

$$\underbrace{\begin{bmatrix} t_{n,i} \\ t_{n+1,i} \\ \vdots \\ t_{m,i} \end{bmatrix}}_{\mathbf{t}} = \underbrace{\begin{bmatrix} l_{n,i} \\ l_{n+1,i} \\ \vdots \\ l_{m,i} \end{bmatrix}}_{\mathbf{L}} \underbrace{\begin{bmatrix} s_i \end{bmatrix}}_{\mathbf{S_T}} \tag{5}$$

where i is the time index, and m and n are depth indices, $t_{n,i}$ is the lagtime between the signal from the reference depth, and the signal at the depth of interest, for a given time in the record, $l_{n,i}$ is the distance between the reference depth and depth of interest, and s_i is the apparent thermal slowness, where thermal slowness is defined as the inverse of thermal velocity. Thermal slowness is used in order to keep the inverse problem in equation 5 linear. Given the above equation, we can solve for lagtime as a function of thermal slowness. Using a standard least-squares formulation, we solve equation 6 for the thermal slowness, given a series of lagtimes, as follows:

$$\mathbf{S_T} = \left(\mathbf{L^T} \cdot \mathbf{W^T} \cdot \mathbf{W} \cdot \mathbf{L}\right)^{-1} \mathbf{L^T} \cdot \mathbf{W^T} \cdot \mathbf{W} \cdot \mathbf{t} \tag{6}$$

where W is a diagonal matrix that contains the inverse of the standard deviation of the lagtimes. We can define the covariance matrix for $\mathbf{S}_\mathrm{T}$ as follows (Tarantola,1987):

$$\mathbf{C_S} \approx \left(\mathbf{L^T} \cdot \mathbf{W^T} \cdot \mathbf{W} \cdot \mathbf{L}\right)^{-1}. \tag{7}$$

From this we can obtain the standard deviation of $\mathbf{S}_T$

$$std(\mathbf{S}_T) = \sqrt{diag(\mathbf{C_s})}\,. \tag{8}$$

We solve both equation 6 and 8 for each time step in the lagtime data set, thus generating a record of thermal slowness, and an error estimate, as a function of time. Thermal slowness is easily then converted to thermal velocity ($\mathbf{V}_T$) by taking the reciprocal, where $\mathbf{V}_T = \dfrac{1}{\mathbf{S}_T}$.

3.3 Estimating Infiltration Rate

Hatch et al. (2006) present a solution for calculating the infiltration rates based on the phase lag of a thermal signal, calculated between two vertically aligned temperature sensors.

Upon inspection of their solution, it becomes clear that for thermal velocities greater than ~1 m/d, advection dominates and the thermal velocity can be taken as equal to the advective velocity of the thermal signal. Given the advective thermal velocity, one can calculate the velocity of the associated fluid infiltration front as:

$$\mathbf{V}_f = \frac{\rho c}{\rho_f c_f} \mathbf{V}_T \qquad (9)$$

where $\rho_f c_f$ is the heat capacity of the fluid, ρc is heat capacity of the saturated sediment - fluid system. For this work we use values from Hopmans et al. (2002), for the heat capacity of the fluid and dry sediment, of 4.186x10^6 $\frac{J}{{}^oC \bullet m^3}$ and 1.92 x10^6 $\frac{J}{{}^oC \bullet m^3}$, respectively. Using the relationship from Campbell et al. (1991):

$$\rho c = \phi \cdot \rho_f c_f + (1-\phi) \cdot \rho_q c_q \qquad (10)$$

where ϕ is porosity, assumed to be 35%, ρ_q is the density of quartz, and c_q is the heat capacity of quartz. Evaluating equation 10, yields a heat capacity of the saturated sediment of: ρc=2.82x10^6 $\frac{J}{{}^oC \bullet m^3}$.

4. Results and conclusions

Figure 8 presents the results of our inversion and infiltration velocity calculation. In Figure 8a we have the calculated infiltration rate at the probe along with error estimates, obtained using equation 8. In Figure 8b, we have the estimated standard deviation of our data normalized by the measured lagtime. For this analysis we assume that the lagtimes have a standard deviation of 1/2 of a sampling interval (e.g. 15min), so that 95% of our measured lagtimes fall within +/- one sampling interval. We note this model is optimistic in terms of true data errors, as it only addresses the issue of temporal sampling. As is seen the Figure 8b, we have significantly higher relative error in the near surface; incorporating this information into our inversion, allows us to fit the deeper, more precise data, to a higher tolerance. Figure 8c shows the error between the predicted lagtimes, given the velocity model in Figure 8a, and the true lagtimes, presented as a percent of true lagtimes. As with Figure 8b, we see higher error towards the top of the model with lower error towards the bottom. We note that Figure 8c is not expected to be a perfect reproduction of Figure 8b. This is because the predicted data used in Figure 8c represent the best fit model, whereas the error model in Figure 8b represents that error for a model that is biased by one standard deviation.

Figure 8 (a) Estimated infiltration rate from inversion (solid line), and the 95% confidence intervals (dashed line); (b) standard deviation of lagtimes normalized by measured lagtimes; (c) Error between predicted lagtimes and true lagtimes, normalized by true lagtime.

In Figure 9, we present the results of our analysis, the estimated values of the infiltration rate, along with the average infiltration rate calculated for the entire pond during the same time window. The estimated infiltration rate at our probe location is significantly higher than the average rate for the pond. It is not surprising to find spatial variability in infiltration rates, across the base of the pond. Given that our probe was located at the lowest point in the pond, which would have a larger hydraulic gradient than other locations, we would expect to see a higher infiltration rate. What is more interesting is the fact that infiltration at the probe steadily decreases with time, while the average rate actually sees an increase over this time period. We attribute this to a change in the area covered by the pond at approximately 600 h. At this time the pond reached the height here it began to flood the outer flanks of the pond. This new area had not yet been subjected to clogging. Therefore the average infiltration rate for the pond continues to increase, despite the fact that the inner part of the pond is clogging. We note, that the mass balance estimate presented here does not contain an error estimate. However, we do not anticipate the errors in the calculation would be large enough to account for the disparity between the two measures; for example we would require a factor of four error in pumping rates to explain this discrepancy.

Figure 9 Estimated infiltration rate from inversion (solid black line), and the 95% confidence intervals (dashed black line), Solid red line is the mass balance infiltration rate..

The diurnal temperature change in a body of surface water can produce a thermal signal that provides a way of monitoring the infiltration of surface water into the subsurface. In this study we have demonstrated the value of using wavelet analysis to isolate and analyze the signal associated with this diurnal forcing. The approach that we have used is ideally suited for analysis of non-stationary signals and thus is an effective way to analyze temperature data or, as in our case, resistivity data. One important issue that requires further work is improved understanding of the uncertainty in the derived estimates of infiltration rates. Our inversion algorithm incorporates a data weighting term, and from this, error estimates of infiltration rates. However, the value of these error estimates is predicated on our ability to assess actual data errors. Given this issue one must view the error estimates of the infiltration rates with caution. In this work we have only considered error from the sampling intervals, there are however two other sources of error that could be considered. First, calculating phase in the wavelet domain introduces error in a complicated way that is dependent on the: 1) non-stationarity of the signal under consideration, 2) the intrinsic noise in the measured signal, and 3) the range of wavelet periods that are considered. The second type of error we have not considered is modelization error introduced when transforming calculated lagtimes into infiltration velocities. In this paper, the modelization assumptions include: 1) inverting for a one-dimensional thermal velocity as a function of time and 2) the use of the Hatch et al. model to convert the thermal velocity to infiltration rate. One approach for ascertaining the magnitude of these error sources, would be to use synthetic modeling of the signal/system under consideration. Future work in this direction is necessary to avoid overly optimistic error estimates.

The key finding of our study is the presence of the diurnal temperature signal in resistivity data. A measurement of resistivity has a significant advantage over a measurement of temperature. A temperature measurement is a point measurement made at the location of the sensor. A resistivity measurement can be made using spaced electrodes that sample an undisturbed, or less disturbed, region of the subsurface. In the case of the probe used in this field experiment, the resistivity measurements sampled a region tens of centimeters from the probe, while the temperature measurements were made at the probe. It is very likely that fluid flow at the temperature probe was highly affected by the disturbance of the sediments during the emplacement of the probe. An appealing extension of this study is to investigate whether the diurnal temperature signal can be seen in resistivity data acquired using surface electrodes or cross borehole arrays, thus providing a minimally invasive means of quantifying infiltration rates and variability over subsurface regions on the scale of tens of meters. This would provide a new, much-needed way of capturing information about spatial and temporal variation in infiltration processes.

Acknowledgments

This research was supported by funding to R. Knight from Schlumberger Water Services. We wish to thank Brian Lockwood, Mary Bannister and others from the Pajaro Valley Water Management Agency. We also thank Andy Fisher, Andrew Racz and Calla Schmidt, from UCSC, for providing us with the pond volume to area function used to calculate the mass balance infiltration rate. We also thank the comments of three anonymous reviewers as well as the Associate editor, Alex Furman, for their comments and criticisms of this manuscript.

References:

Brassington, R. 1998 , Field Hydrogeology. (2nd edn. ed.),, Wiley, England (1998).

Campbell, G.S., Calissendorff, C., and Williams, J. H. 1991. Probe for measuring soil specific heat using a heat-pulse method. Soil Science Society of America Journal, 55(1): 291-293.

Constantz, J. .2008. Heat as a tracer to determine streambed water exchanges, Water Resour. Res., 44, W00D10, doi:10.1029/2008WR006996.

Constantz, J., and Stonestrom D.A. 2003. Heat as a tracer of water movement near streams, in Heat as a Tool for Studying the Movement of Ground Water Near Streams, edited by D. A. Stonestrom and J. Con- stantz, U.S. Geol. Surv. Circ., 1260, 1 – 63.

Grinsted, A., Moore J.C. and Jevrejeva, S. 2004. Application of the cross wavelet transform and wavelet coherence to geophysical time series, *Nonlinear Processes Geophys.*, 11(5/6): 561–566.

Hatch C.E., Fisher A.T., Revenaugh J.S., Constantz J. and Ruehl C. 2006. Quantifying surface water groundwater interactions using time series analysis of streambed thermal records: Method development. Water Resour. Res. 42: W10410, doi: 10.1029/2005WR004787.

Henderson, R.D., Day-Lewis, F.D. and Harvey C.F. 2009. Investigation of aquifer-estuary interaction using wavelet analysis of fiber-optic temperature data Geophys. Res. Lett. 36: L06403, doi:10.1029/2008GL036926.

Hopmans J.W., Simunek J. and Bristow K.L. 2002. Indirect estimation of soil thermal properties and water flux using heat pulse probe measurements: Geometry and dispersion effects. Water Resour. Res. 38:1.

Izbicki, J.A., Flint, A. L., and Stamos, C. L. 2008. Artificial recharge through a thick, heterogeneous unsaturated zone. Ground water, 46(3): 475-488.

Izbicki, J.A., Johnson, R.U., Kulongoski, J, and Predmore, S. 2007, Ground-water recharge from small intermittent streams in the western Mojave desert, California. In: Ground-water recharge in the arid and semi-arid southwestern United States, ed. Stonestrom, D.A., Constantz, J., Ferré, T.P.A., Leake, S.A. U.S. Geological Survey Professional Paper 1703. Reston, Virginia: USGS.

Keery J., Binley A., Crook N. and Smith J.W.N. 2007. Temporal and spatial variability of groundwater-surface water fluxes: Development and application of an analytical method using temperature time series. Journal of Hydrology 336:1-16.

Knight, R., and Endres, A.L. 2005. An introduction to rock physics for near-surface applications in Near-surface geophysics, volume 1: Concepts and fundamentals. ed, Butler, D., Society of Exploration Geophysicists, 31-70.

Kumar. P., and Foufoula-Georgiou E. 1997. Wavelet analysis for geophysical applications, *Reviews of Geophysics*, 35(4): 385-412.

Labat, D., 2010. Cross wavelet analyses of annual continental freshwater discharge and selected climate indices. Journal of Hydrology 385: 269-278.

Labat, D., 2008. Wavelet analysis of the annual discharge records of the world's largest rivers. Adv. Water Resour. Res. 31: 109–117.

Lesmes D.P. and Friedman S.P. 2005. Relationships between the electrical and hydrogeological properties of rocks and soils. Hydrogeophysics 87-128.

Racz. A., Fisher, A., Lockwood, B., Los Huertos, M., Schmidt, C.. Lear, J. 2008 Quantifying the Distribution and Dynamics of Managed Aquifer Recharge Using Mass- Balance and Time-Series Thermal Methods *89*(53), Fall Meet. Suppl., Abstract H13A-0888.

Tarantola, A. 1987. Inverse problem theory: Methods for data fitting and model parameter estimation. Elsevier Science Ltd, Oxford.

Telford W.M.M., Geldart L.P. and Sheriff R.E. 1990. Applied geophysics. Cambridge University Press, Cambridge.

Torrence, C., and Compo, G. P. 1998 A practical guide to wavelet analysis, *Bull. Am. Meteorol. Soc.*, 79: 61– 78.

Harkins Slough Infiltration Pond

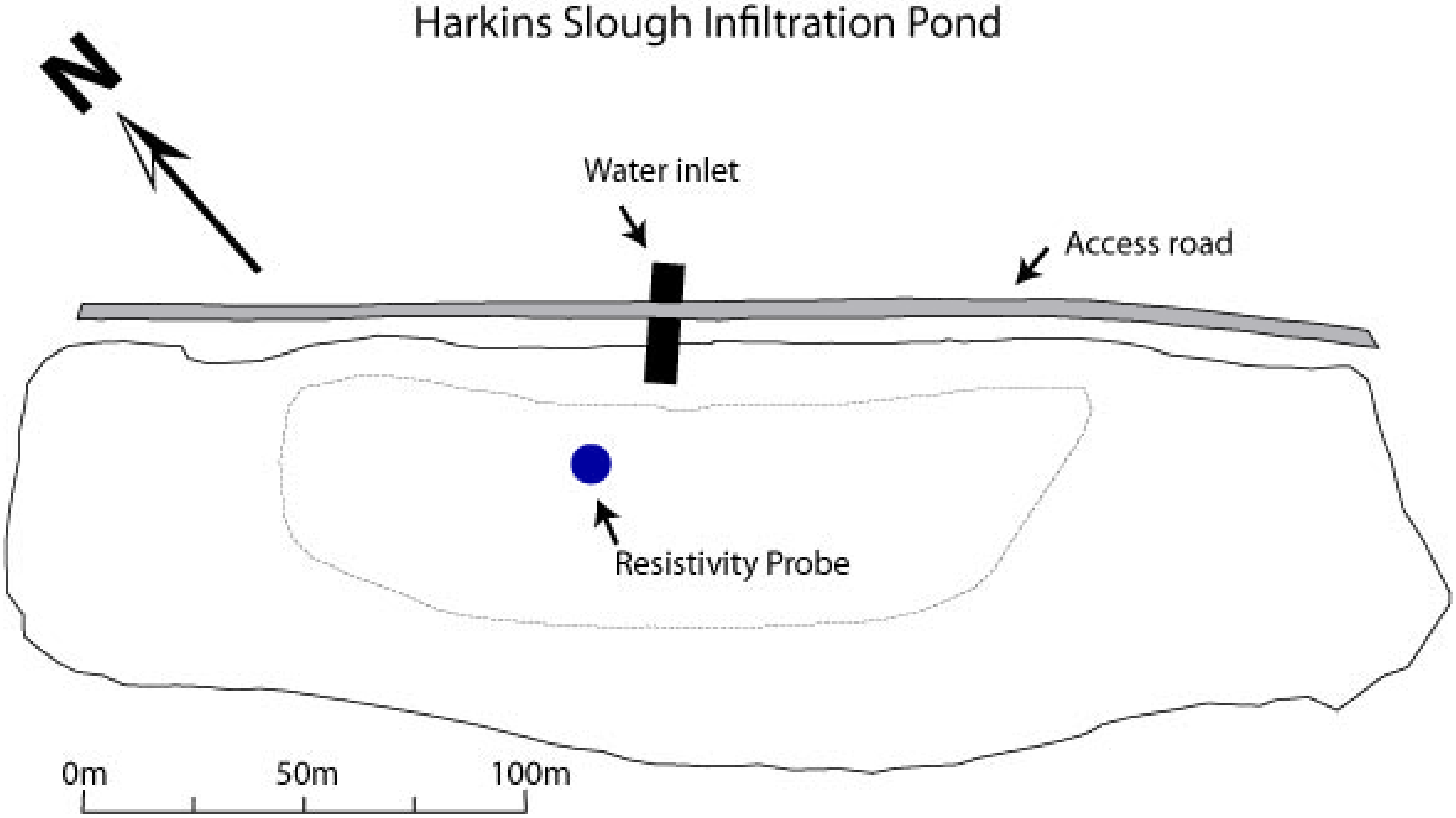

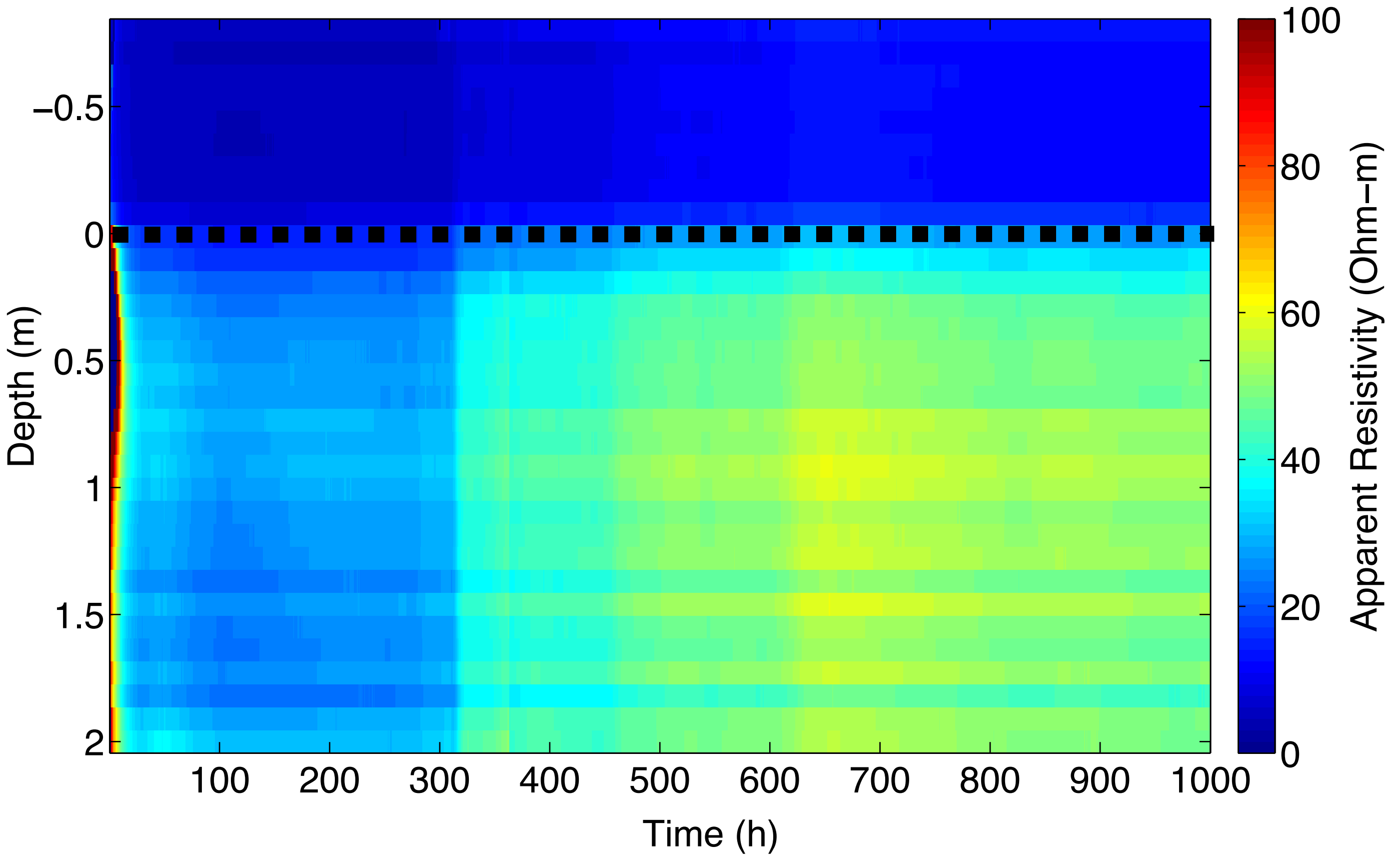

−0.5
0
0.5
1
1.5
2
Depth (m)
100
200
300
400
500
600
700
800
900
1000
Time (h)
100
80
60
40
20
0
Apparent Resistivity (Ohm−m)

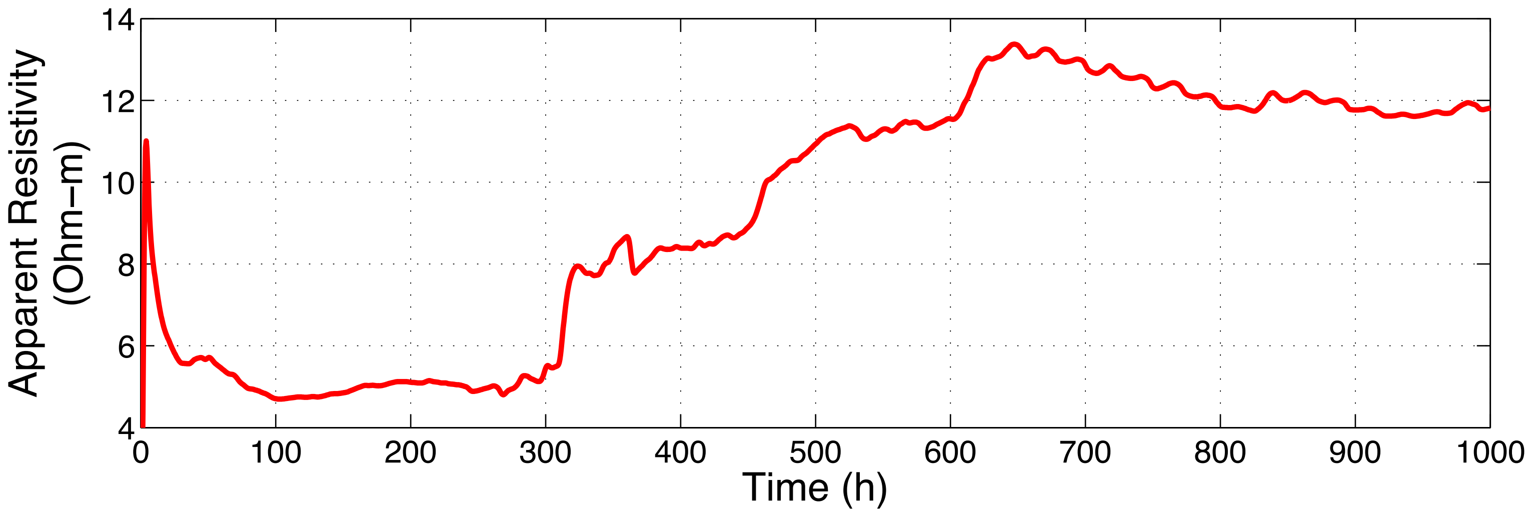
Apparent Resistivity
(Ohm−m)
14
12
10
8
6
4
0
100
200
300
400
500
600
700
800
900
1000
Time (h)

(a)

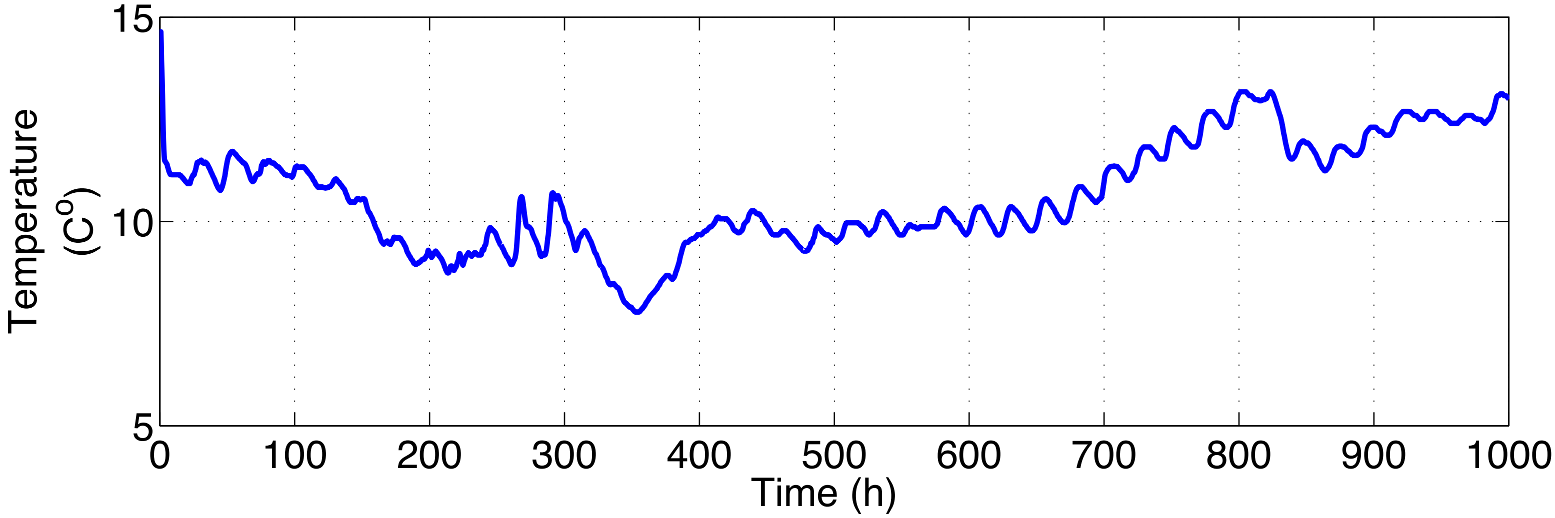
Temperature
(C^o)
15
10
5
0
100
200
300
400
500
600
700
800
900
1000
Time (h)

(b)

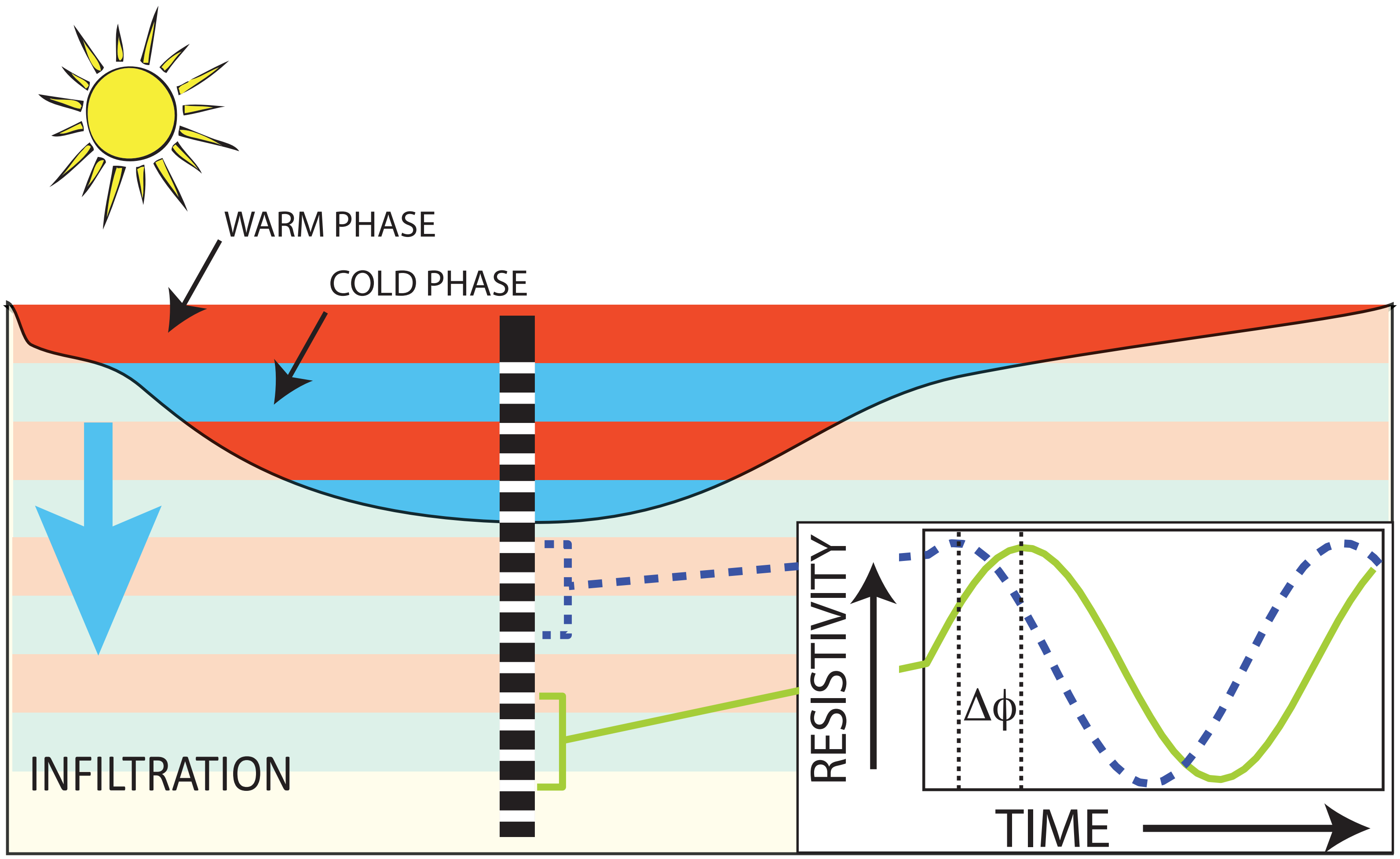

WARM PHASE
COLD PHASE
INFILTRATION
RESISTIVITY
Δφ
TIME

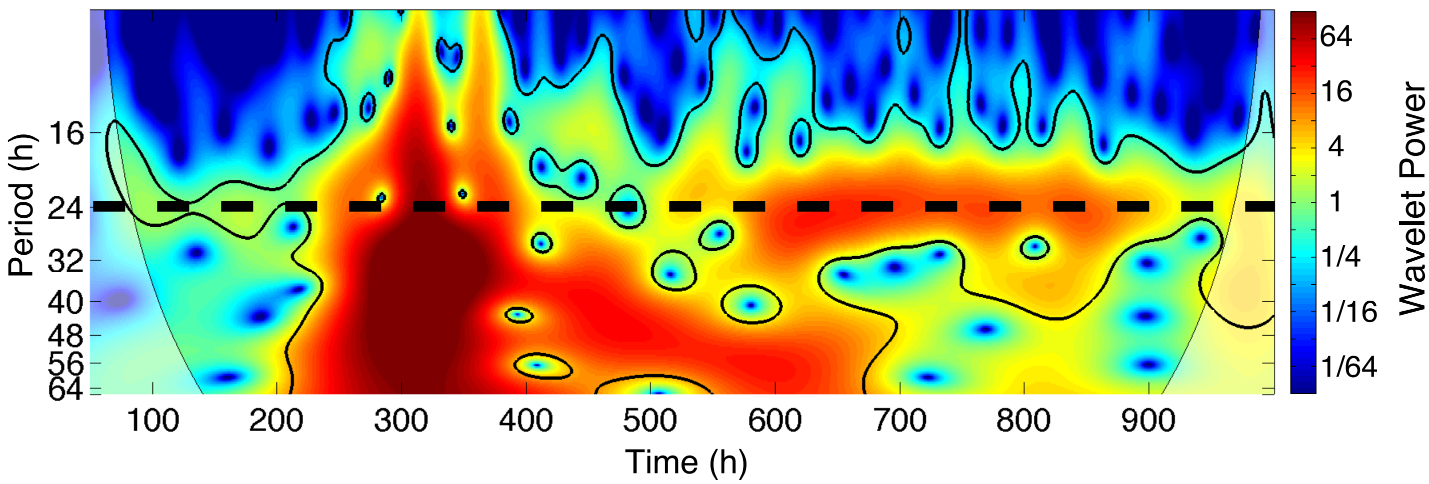

Period (h)
16
24
32
40
48
56
64
100
200
300
400
500
600
700
800
900
Time (h)
64
16
4
1
1/4
1/16
1/64
Wavelet Power

(a)

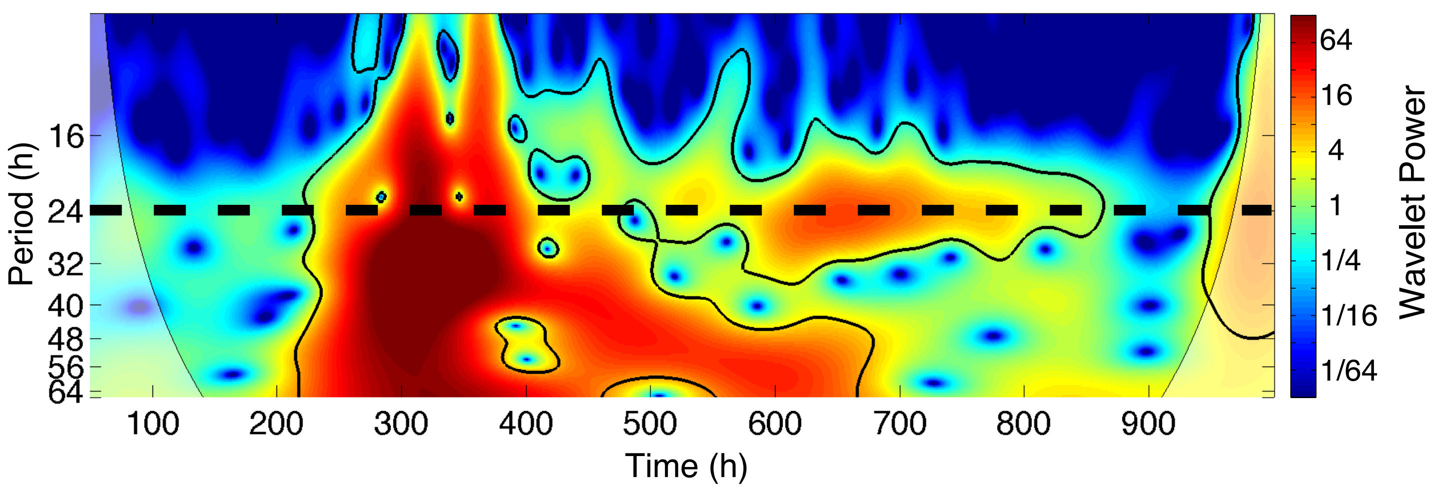

Period (h)
16
24
32
40
48
56
64
100
200
300
400
500
600
700
800
900
Time (h)
64
16
4
1
1/4
1/16
1/64
Wavelet Power

(b)

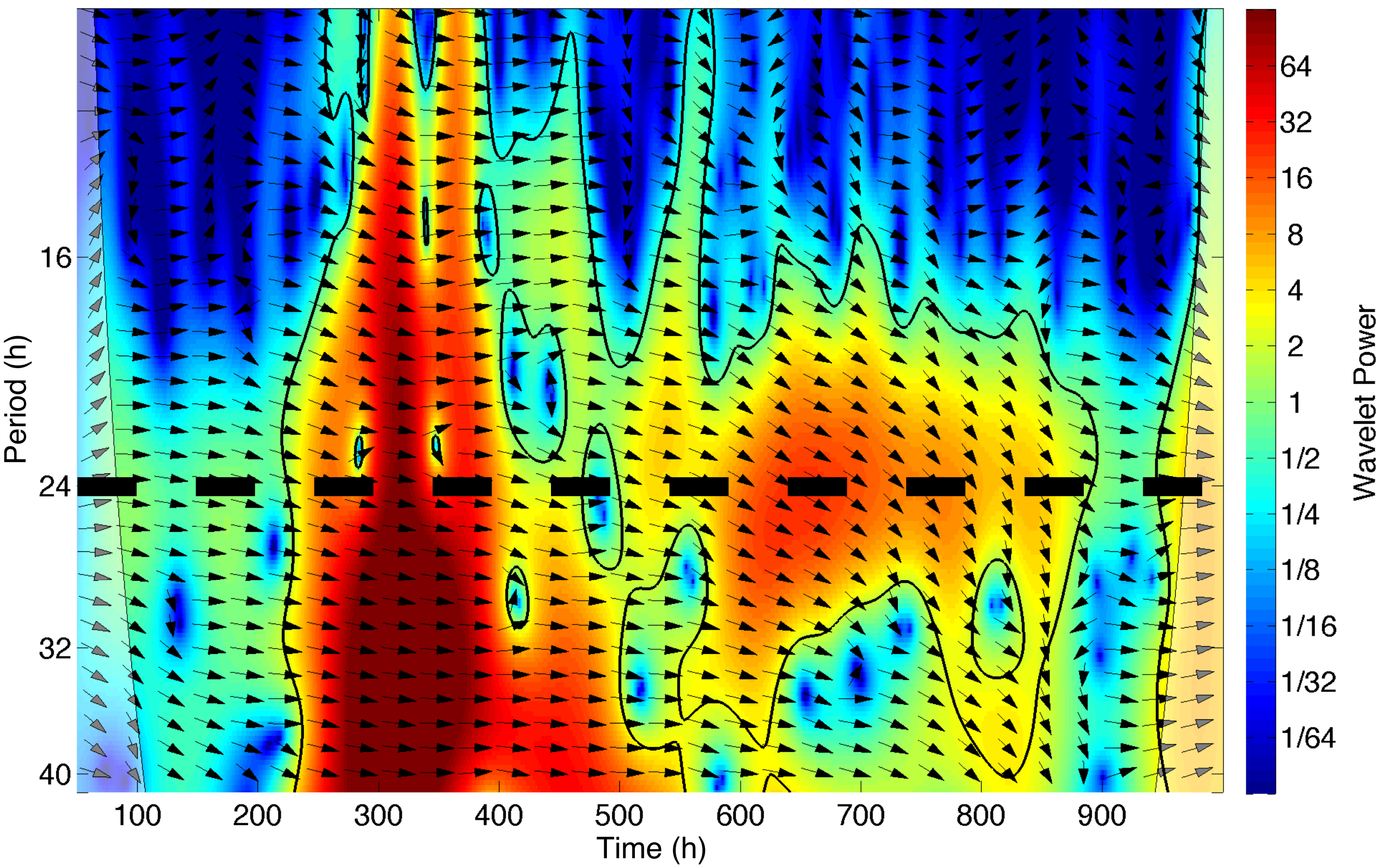

Period (h)
16
24
32
40
100
200
300
400
500
600
700
800
900
Time (h)
64
32
16
8
4
2
1
1/2
1/4
1/8
1/16
1/32
1/64
Wavelet Power

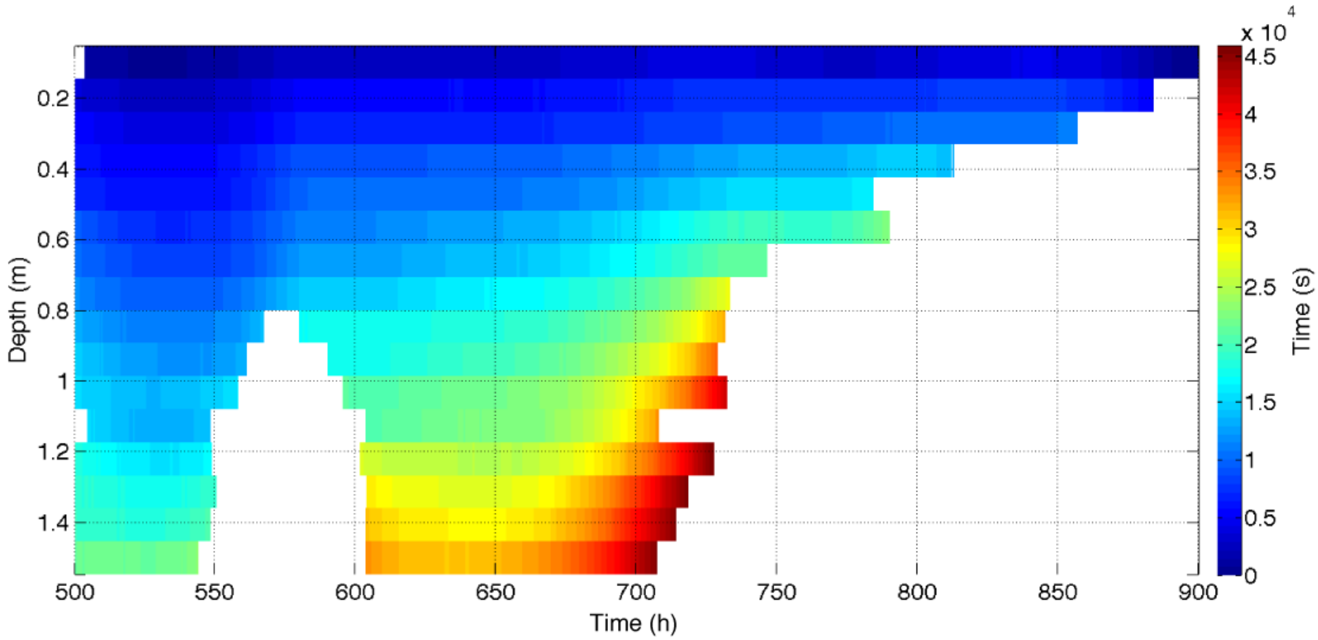

Depth (m)
0.2
0.4
0.6
0.8
1
1.2
1.4
500
550
600
650
700
750
800
850
900
Time (h)
x 10^4
4.5
4
3.5
3
2.5
2
1.5
1
0.5
0
Time (s)

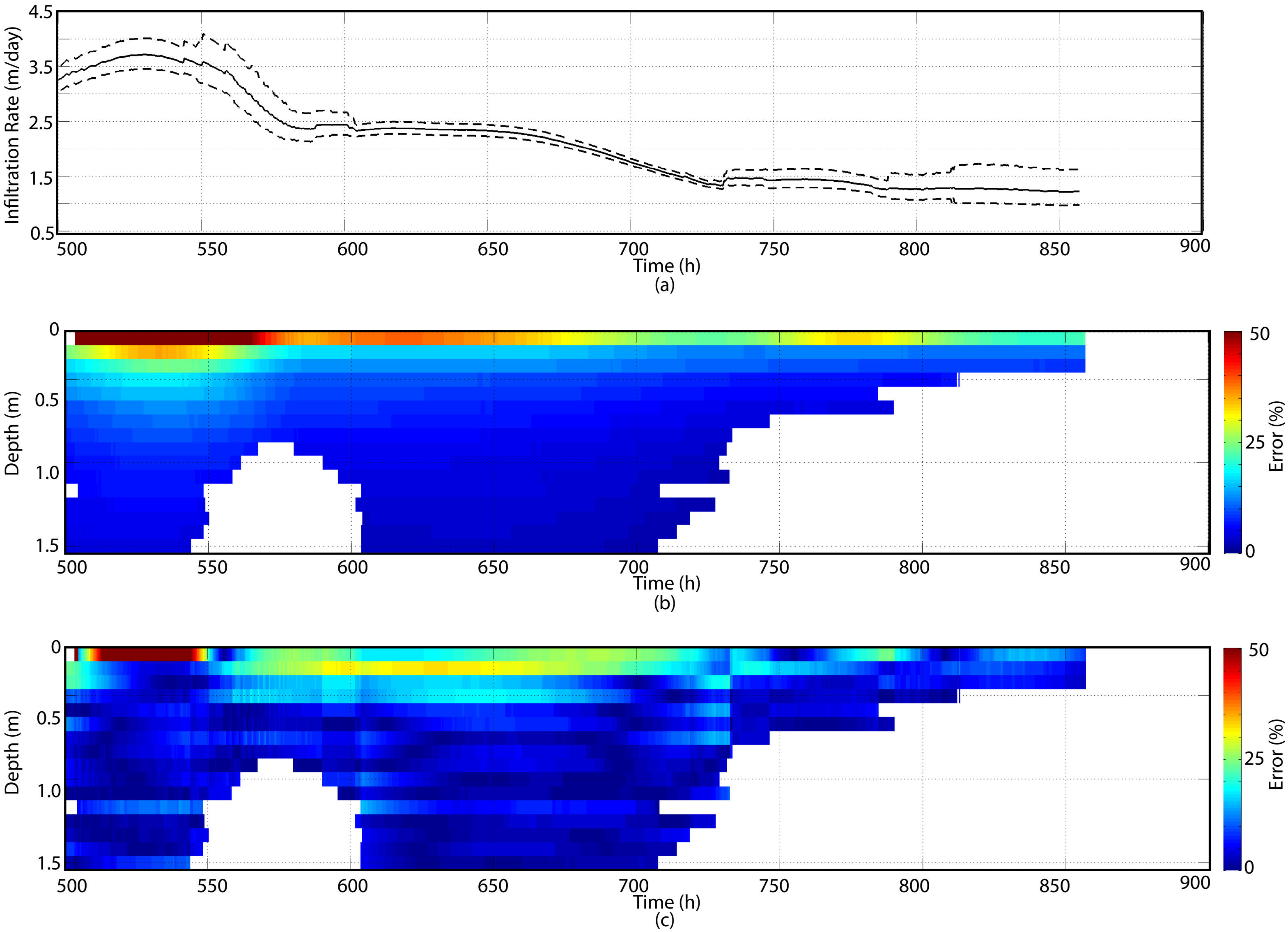
Infiltration Rate (m/day)
4.5
3.5
2.5
1.5
0.5
500
550
600
650
700
750
800
850
900
Time (h)
(a)
Depth (m)
0
0.5
1.0
1.5
Error (%)
50
25
0
Time (h)
(b)
Time (h)
(c)

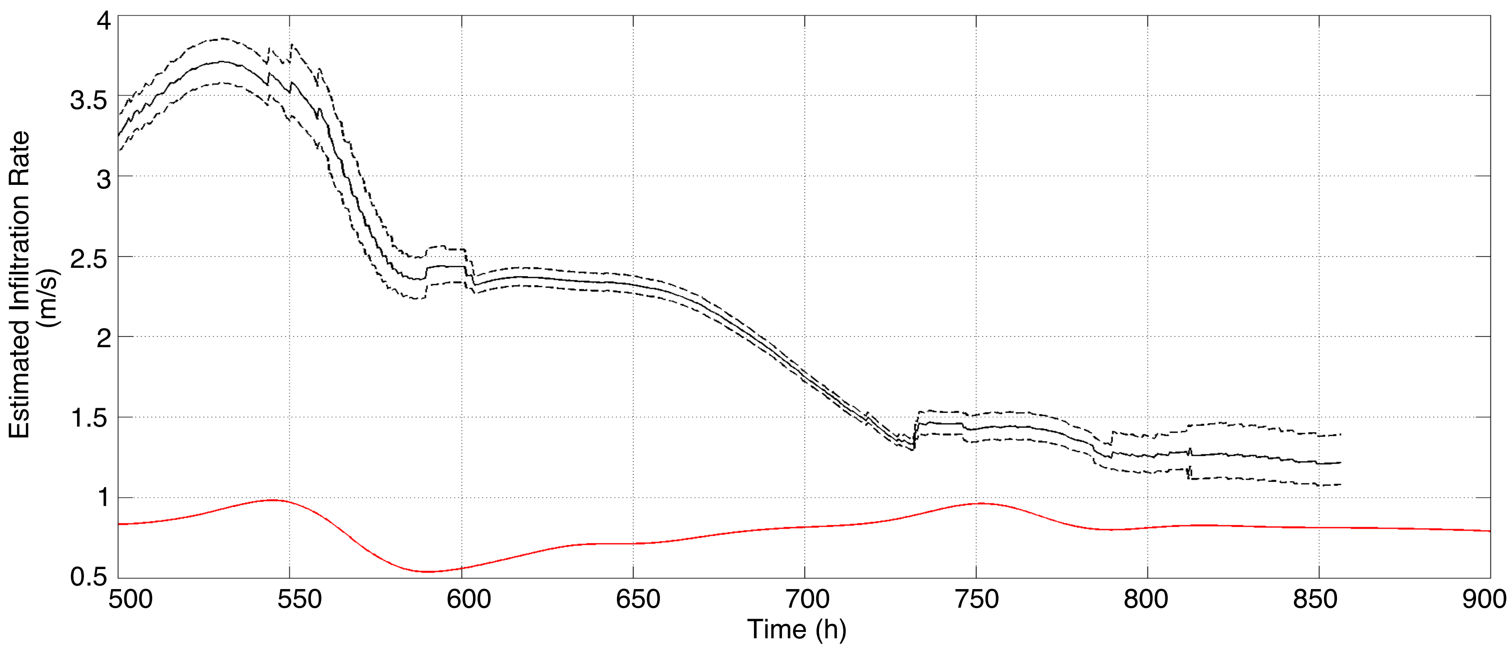

Estimated Infiltration Rate (m/s)
Time (h)
0.5
1
1.5
2
2.5
3
3.5
4
500
550
600
650
700
750
800
850
900